Research Square

Preprints are preliminary reports that have not undergone peer review.
They should not be considered conclusive, used to inform clinical practice,
or referenced by the media as validated information.

Decoupling compaction density from interfacial kinetics in LiFePO 4 /C cathodes: coupled restructuring across scales and charge-transfer barrier lowering through re-sintering

Chang Liu
Lanzhou University of Technology
Tingzhi Feng
Lanzhou University of Technology
Yanshuang Meng
Lanzhou University of Technology
Fuliang Zhu
chzfl@126.com

Lanzhou University of Technology

Research Article

Keywords: LiFePO4/C, re-sintering, apparent charge-transfer activation energy, bimodal particle size distribution, powder compaction density

Posted Date: November 25th, 2026

DOI: https://doi.org/10.21203/rs.3.rs-11773064/v1

License: This work is licensed under a Creative Commons Attribution 4.0 International License.
Read Full License

Additional Declarations: No competing interests reported.

Decoupling compaction density from interfacial kinetics in $LiFePO_4$/C cathodes: coupled restructuring across scales and charge-transfer barrier lowering through re-sintering

Chang Liu[a], Tingzhi Feng[a], Yanshuang Meng*[bc], Fuliang Zhu*[ab]

a State Key Laboratory of Advanced Processing and Recycling of Non-ferrous Metals, Lanzhou University of Technology,Lanzhou 730050, China

b School of Metallurgy and Environment, Lanzhou University of Technology, Lanzhou 730050, China

c Key Laboratory of Advanced Energy Materials Chemistry (Ministry of Education), Nankai University, Tianjin 300071, China

*Corresponding author. E-mail:

mengyanshuang@163.com (Yanshuang Meng)

chzfl@126.com (Fuliang Zhu)

Abstract:

The high-rate performance of $LiFePO_4$/C (LFP/C) is closely associated with interfacial reaction kinetics, making the simultaneous optimization of compaction density and electrochemical performance an important objective. Here, LFP/C was prepared from $Fe_3(PO_4)_2$, Li_3PO_4, and glucose. With identical starting-material ratios and carbon-source inputs, the once-sintered sample (LFP-1S) was subjected to an additional cooling–reheating treatment to obtain LFP-2S. Re-sintering transformed a predominantly unimodal particle size distribution centered at 1.16 μm into a bimodal distribution, with D_{50} increasing from 1.33 to 1.98 μm. A four-size-class geometric packing model predicted an increase in packing fraction from 0.710 to 0.741, while the measured powder compaction density increased from 2.52 to 2.58 $g \cdot cm^{-3}$. Meanwhile, the Brunauer–Emmett–Teller (BET) specific surface area decreased from 13.88 to 9.554 $m^2 \cdot g^{-1}$, whereas both the interfacial charge-transfer resistance and the apparent activation energy decreased, the latter from 22.7 to 20.8 $kJ \cdot mol^{-1}$. The discharge specific capacity at 0.1 C increased from 146 to 160 $mAh \cdot g^{-1}$, and the discharge specific capacity after 100 cycles increased from 145 to 161 $mAh \cdot g^{-1}$. The overall improvement in kinetics despite a 31.2% decrease in BET specific surface area indicates more favorable interfacial charge-transfer and Li^+ transport responses after re-sintering. Re-sintering simultaneously produces a bimodal particle size distribution and improves powder packing and interfacial kinetics, enabling the coordinated enhancement of compaction density and electrochemical performance.

Keywords: $LiFePO_4$/C; re-sintering; apparent charge-transfer activation energy; bimodal particle size distribution; powder compaction density

1 Introduction

Since Padhi et al. reported olivine-type lithium iron phosphate ($LiFePO_4$, LFP) as a cathode material for lithium-ion batteries [1], its safety, low cost, and long cycle life have supported its use in traction batteries and stationary energy storage. Increasing volumetric energy density requires improvements in both powder packing and active-material utilization. Tap density, powder compaction density measured at a specified pressure, and coating density after electrode calendering are distinct physical quantities and should be distinguished according to their measurement conditions [2,3]. Particle refinement shortens solid-state diffusion paths and increases the specific surface area, whereas efficient powder packing, processability, and interfacial stability impose different requirements on particle organization. Coordinated optimization of compaction density and reaction kinetics is therefore an important research objective.

The rate capability of $LiFePO_4$/carbon (LFP/C) depends on electronic conduction, Li^+ diffusion, interfacial charge transfer, and electrode microstructure. Strategies such as carbon coating, elemental doping, and particle structure design [4–9] improve electrochemical performance by establishing conductive networks, modifying crystal and interfacial structures, and shortening transport paths. Prosini et al. investigated lithium chemical diffusion using galvanostatic intermittent titration and impedance measurements, providing a methodological basis for evaluating transport during lithium intercalation and deintercalation [10]. Specific surface area measurements characterize gas adsorption by the powder, whereas the electrochemical response is closely associated with electrolyte wetting, electronic connectivity, and the state of the reactive interface. Analyzing changes in specific surface area together with charge transfer, diffusion, and rate capability helps relate particle organization to electrochemical performance.

The heat-treatment protocol is an important processing variable for controlling reaction progress, particle growth, and carbon-layer evolution [11]. Re-sintering previously formed LFP/C can further modify particle contacts, agglomeration, and the particle size distribution. Reheating after cooling and the additional holding stage together constitute the re-sintering treatment. Previous studies have examined

precursor morphology [12], ternary solid-state synthesis [13], pre-agglomeration granulation and fluidized-bed sintering [14], hydrothermal conditions [15], and particle size distribution control and packing-density modeling [16–19]. These studies establish relationships among preparation conditions, particle organization, and dense packing, providing a basis for using heat treatment to improve powder properties and electrochemical response together.

Electrode-level studies also demonstrate close relationships between particle p acking and transport behavior. Studies of compaction processing [20], conductive interfacial components [21], plate-like particles with low specific surface areas [2 2], and transport regulation in thick electrodes [23,24] indicate that material morp hology, packing structure, and charge transport should be designed together. Exa mining changes in specific surface area alongside interfacial charge-transfer and d iffusion parameters therefore provides a more comprehensive understanding of str ucture–property relationships in LFP/C.

In this study, LFP/C was prepared from $Fe_3(PO_4)_2$, Li_3PO_4, and glucose. A portion of the once-sintered material from the same batch was reheated after cooling and subjected to an additional holding stage to obtain the re-sintered sample, LFP-2S. The once-sintered sample, LFP-1S, served as the reference for evaluating the effects of this additional heat treatment on powder structure and electrochemical response. X-ray diffraction (XRD), scanning electron microscopy (SEM), energy-dispersive X-ray spectroscopy (EDS), laser particle size analysis, specific surface area measurements, and powder compaction tests were used to characterize crystal structure, particle organization, and packing behavior. A simplified geometric packing model was used to interpret the density changes. Electrochemical performance was evaluated using galvanostatic charge–discharge, rate capability and cycling tests, cyclic voltammetry (CV), electrochemical impedance spectroscopy (EIS), and temperature-dependent EIS. After re-sintering, the Brunauer–Emmett–Teller (BET) specific surface area decreased by 31.2%, the powder compaction density increased from 2.52 to 2.58 $g \cdot cm^{-3}$, the interfacial charge-transfer resistance decreased, and the apparent activation energy decreased from 22.7 to 20.8 $kJ \cdot mol^{-1}$. Both CV and EIS yielded higher apparent Li^+

diffusion coefficients. These results demonstrate the combined effects of re-sintering on particle packing and interfacial kinetics, showing that improvements in particle size distribution and electrode transport response enable simultaneous increases in compaction density and electrochemical performance.

2 Materials and methods

2.1 Material preparation

LFP/C samples with different thermal histories were prepared using identical starting-material ratios and carbon-source inputs to investigate the effects of re-sintering on particle organization, powder compaction, and electrochemical performance. Iron(II) phosphate ($Fe_3(PO_4)_2$), lithium phosphate (Li_3PO_4), and glucose ($C_6H_{12}O_6$) were used as the starting materials. $Fe_3(PO_4)_2$ and Li_3PO_4 were mixed at a molar ratio of 1:1, and 6 wt% glucose was added as the carbon source. The mixture was ball-milled in anhydrous ethanol at 400 rpm for 6 h using a planetary ball mill and then dried to obtain a mixed precursor. The precursor was placed in an alumina crucible, heated under Ar at 5 °C·min^{-1} to 400 °C, and held for 4 h for pre-carbonization. It was then heated at the same rate to 740 °C and held for 10 h, followed by furnace cooling to room temperature, to obtain LFP-1S. A portion of LFP-1S was reheated under Ar at 5 °C·min^{-1} to 740 °C, held for 6 h, and furnace-cooled to room temperature to obtain LFP-2S. The preparation procedure is illustrated in Fig. 1. No additional carbon source or other additives were introduced during re-sintering. Both samples had identical initial starting-material ratios and carbon-source inputs.

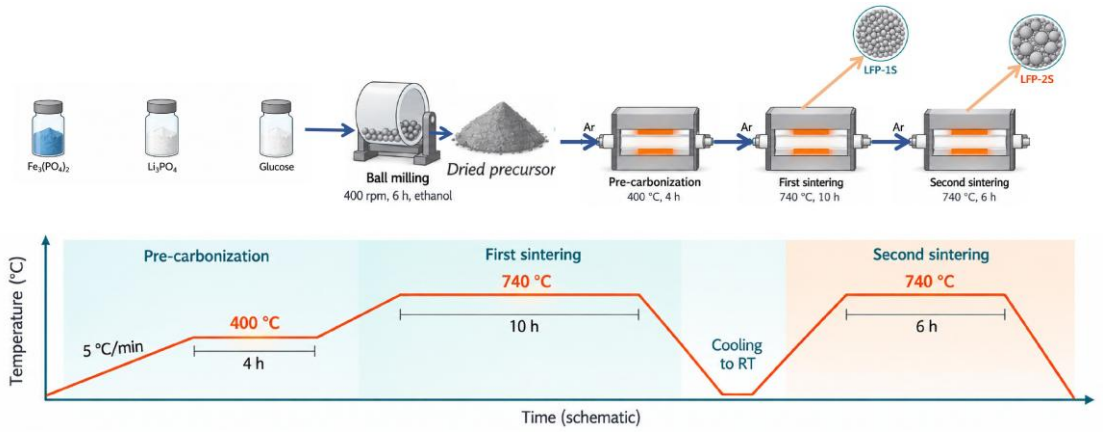

Fig. 1 Schematic illustration of the preparation of LFP-1S and LFP-2S

2.2 Material characterization

The crystal structure was analyzed by powder XRD using Cu Kα radiation (λ = 0.15418 nm) at 40 kV and 30 mA. Data were collected at 25 °C over a 2θ range of 10°–80° at a scan rate of $10°\cdot min^{-1}$. Rietveld refinement was used to obtain lattice parameters and evaluate agreement between the calculated and experimental diffraction patterns. Particle morphology and elemental distributions were examined by SEM and EDS. Volume-based particle size distributions were measured by laser particle size analysis. D_{10}, D_{50}, D_{90}, and the distribution width were extracted to characterize changes in particle size distribution before and after re-sintering. Powder compaction tests were conducted at 300 MPa with a holding time of 30 s. The compaction density was calculated as $\rho = m/(A\cdot h)$, where m is the powder mass, A is the cross-sectional area of the compact, and h is its thickness in the corresponding measurement state. A geometric packing model with four size classes was constructed from the measured particle size distributions to estimate the packing fraction γ for comparison with the measured powder compaction density.

2.3 Cell assembly and electrochemical measurements

LFP/C composite powder, poly(vinylidene fluoride) (PVDF), and acetylene black were mixed at a mass ratio of 8:1:1 in N-methyl-2-pyrrolidone (NMP) to prepare a slurry. The slurry was coated onto aluminum foil using a doctor blade with a 75 μm gap, vacuum-dried at 90 °C for 12 h, and punched into disks 12 mm in diameter. The 75

μm value denotes the blade gap. All discharge specific capacities were normalized to the mass of the LFP/C composite powder used. CR2032 half-cells were assembled in an Ar-filled glovebox using lithium metal as the counter electrode. A 50 μL aliquot of electrolyte was added to each side of the separator, giving a total electrolyte volume of 100 μL. The sealed cells were rested for 10 h before testing.

Galvanostatic charge–discharge, rate capability, and cycling tests were performed using a LAND battery testing system at 25 °C over 2.4–4.2 V (vs. Li/Li^+). CV measurements were conducted using an electrochemical workstation over 2.3–4.3 V at scan rates of 0.2, 0.4, 0.6, 0.8, and 1.0 $mV \cdot s^{-1}$. EIS measurements were performed from 100 kHz to 0.01 Hz with an AC perturbation amplitude of 10 mV. The charge-transfer resistance R_{ct} was obtained by equivalent-circuit fitting. Apparent Li^+ diffusion coefficients were calculated from the dependence of the CV peak current on scan rate and from the low-frequency Warburg response in EIS to compare the transport responses of the two samples under the respective measurement conditions and model assumptions. Temperature-dependent EIS measurements were conducted at 25, 35, 45, and 55 °C. An apparent charge-transfer activation energy was obtained by fitting an Arrhenius relationship to characterize the temperature dependence of interfacial charge transfer.

3 Results and discussion

3.1 Morphology and crystal structure

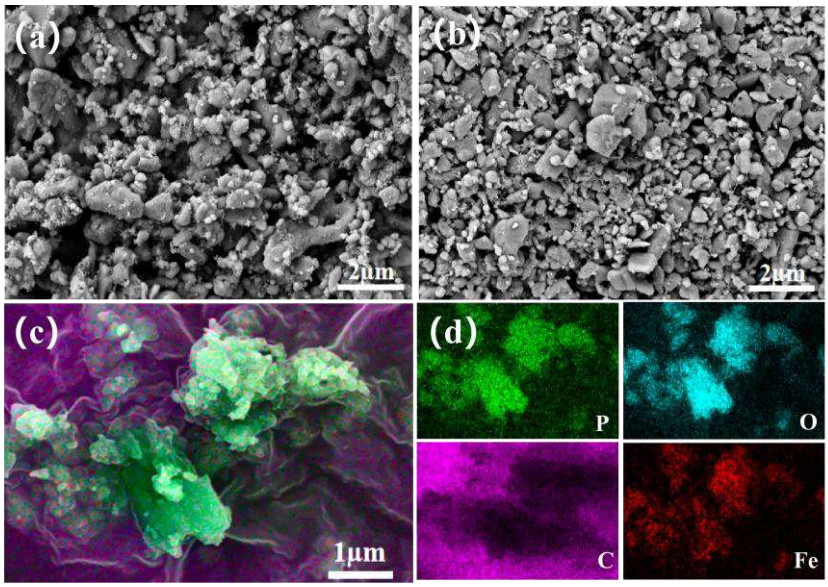

Fig. 2 SEM images and EDS elemental maps of the samples: (a) SEM image of LFP-1S; (b) SEM image of LFP-2S; (c) overlaid EDS elemental map of LFP-2S; and (d) corresponding P, O, C, and Fe elemental maps

Figure 2a,b shows the SEM images of LFP-1S and LFP-2S. Both samples consist of irregular particles and agglomerates, with fine particles of different sizes attached to their surfaces. Compared with LFP-1S, LFP-2S contains some visibly enlarged particles while retaining a population of fine particles, and exhibits closer local particle contacts. The coexistence of coarse and fine particles provides a morphological basis for particle size grading. Fine particles can fill voids between coarse particles, improving powder packing efficiency. Changes in particle size composition and local contact morphology after re-sintering can be related to the measured particle size distribution, specific surface area, compaction density, and electrochemical kinetics.

The overlaid EDS map and individual elemental maps in Fig. 2c,d show that the Fe, P, O, and C signals are mainly distributed over the particle regions, with no evident large-scale elemental segregation. The elements are spatially co-distributed within the observed region, characterizing the elemental distribution of LFP-2S. Together with the SEM observations, the coexistence of coarse and fine particles and closer local contacts provides morphological evidence for improved geometric packing after re-sintering.

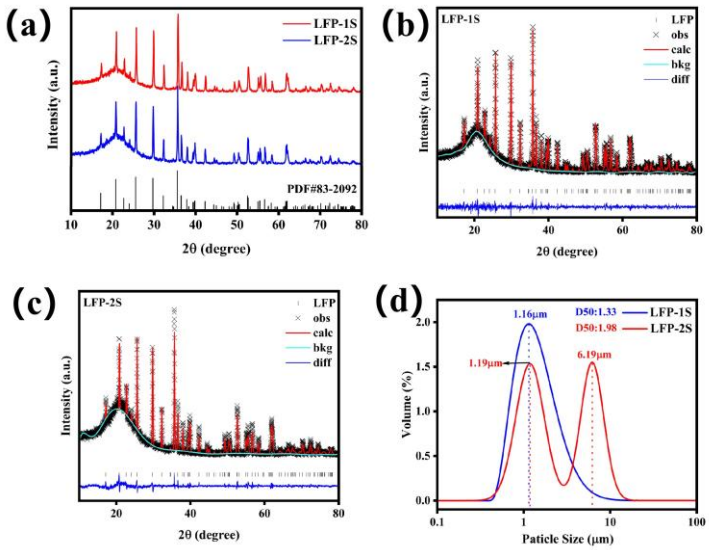

Fig. 3 Crystal structures and particle size distributions of LFP-1S and LFP-2S: (a) XRD patterns of the two samples and reference peak positions of olivine-type $LiFePO_4$; (b,c) Rietveld refinement results for LFP-1S and LFP-2S, respectively; and (d) particle size distributions measured by laser particle size analysis

Figure 3a shows the XRD patterns of the two samples. The main diffraction peaks match the reference peak positions of olivine-type $LiFePO_4$ (PDF 83-2092; orthorhombic system; space group Pnma, No. 62). No characteristic diffraction peaks of impurity phases such as Fe_2O_3, $FePO_4$, or Li_3PO_4 were detected within the measured range, indicating that olivine-type $LiFePO_4$ is the main phase in both samples. LFP-2S retains the characteristic diffraction peaks of LFP-1S after re-sintering. The stable main crystal structure provides a phase basis for comparing the particle organization, powder compaction, and electrochemical behavior of the two samples.

The Rietveld refinement results are shown in Fig. 3b,c and Table 1. The lattice parameters a, b, and c are 10.315, 5.999, and 4.692 Å for LFP-1S and 10.331, 6.006, and 4.693 Å for LFP-2S, respectively. The unit-cell volume increases from 290.373 to 291.191 $Å^3$, corresponding to an increase of approximately 0.28%. The main diffraction peak positions agree with the calculated patterns for both samples. The R_{wp} values of 2.53 and 1.98 indicate good agreement between the refinement models and the experimental diffraction data. The small changes in lattice parameters characterize the average lattice response to the additional heat treatment. Kumar et al. found that Cu

doping had a limited effect on the average crystal structure of LFP, whereas local structural modifications lowered the Li^+ migration barrier and improved diffusion kinetics [25]. Their study identifies the local coordination environment as an important factor linking material structure and ion transport.

Table 1 Lattice parameters of LFP-1S and LFP-2S

Sample	*a* (Å)	*b* (Å)	*c* (Å)	*V* (Å^3)	R_{wp}
LFP-1S	10.315	5.999	4.692	290.373	2.53
LFP-2S	10.331	6.006	4.693	291.191	1.98

3.2 Particle size distribution and compaction density

Table 2 Characteristic particle sizes and BET specific surface areas of LFP-1S and LFP-2S

Sample	D_0 (μm)	D_{10} (μm)	D_{50} (μm)	D_{90} (μm)	D_{100} (μm)	D_{90}/D_{10}	D[4,3] (μm)	BET ($m^2 \cdot g^{-1}$)
LFP-1S	0.406	0.734	1.33	2.94	9.7	4.01	1.66	13.88
LFP-2S	0.461	0.845	1.980	7.91	14.4	9.36	3.33	9.554

Figure 3d and Table 2 show that LFP-1S has a predominantly unimodal distribution with a main mode at approximately 1.16 μm, whereas LFP-2S exhibits two modes at approximately 1.19 and 6.19 μm. D_{10}, D_{50}, and D_{90} denote the particle diameters at cumulative volume fractions of 10%, 50%, and 90%, respectively. D_0 and D_{100} are the reported lower and upper limits of the measured particle size distribution, and D[4,3] is the volume-weighted mean diameter. After re-sintering, D_{50} increases from 1.33 to 1.98 μm, D_{90} from 2.94 to 7.91 μm, D_{90}/D_{10} from 4.01 to 9.36, and D[4,3] from 1.66 to 3.33 μm. Meanwhile, the BET specific surface area decreases from 13.88 to 9.554 $m^2 \cdot g^{-1}$, a decrease of 31.2%.

Re-sintering increases the contribution of the coarse-particle fraction while retaining a fine-particle population, transforming the predominantly unimodal distribution into a bimodal distribution containing both coarse and fine particles. This

change reflects a reorganization of the particles induced by the additional heat treatment. Coarse particles form the main packing framework, while fine particles fill the interstitial voids. Their combination improves geometric packing efficiency, consistent with the particle size grading strategy [19].

To quantify the geometric filling effect of the particle size distribution, a simplified four-size-class model based on linear packing was constructed to estimate the packing fractions and geometric densities of the two samples. The theoretical framework for polydisperse particle packing models can be traced to the work of Stovall et al. [26]. Here, the dominant-size-class relationships and interaction coefficients in the virtual-packing component of the de Larrard framework [27,28] were used to compare geometric packing trends between the samples.

The representative particle diameters are ordered as $d_1 \geq d_2 \geq \ldots \geq d_n$. Here, y_i is the solid volume fraction of size class i, with $\Sigma y_i = 1$, and β_i is its reference packing fraction. When size class i is the dominant class, its estimated packing fraction γ_i and the packing fraction γ of the mixture are given by Eqs. (1) and (2), respectively:

$$\gamma_i = \frac{\beta_i}{1 - \sum_{j<i} W_{ij} y_j - \sum_{j>i} L_{ij} y_j} \tag{1}$$

$$\gamma = \min(\gamma_1, \gamma_2, \cdots, \gamma_n) \tag{2}$$

For a coarser size class j (j < i), the wall-effect coefficient and the corresponding interaction term are defined as follows:

$$b_{ij} = 1 - (1 - \frac{d_i}{d_j})^{1.5} \tag{3}$$

$$W_{ij} = 1 - \beta_i + b_{ij}\beta_i(1 - \frac{1}{\beta_j}) \tag{4}$$

For a finer size class j (j > i), the loosening-effect coefficient and the corresponding interaction term are defined as follows:

$$a_{ij} = \sqrt{1 - (1 - \frac{d_j}{d_i})^{1.02}} \tag{5}$$

$$L_{ij} = 1 - a_{ij}\frac{\beta_i}{\beta_j} \tag{6}$$

The particle size ratios in Eqs. (3) and (5) range from 0 to 1. When the particle diameters are equal, both interaction coefficients approach 1, and the mixture model reduces to the single-size-class case. For comparison under consistent conditions, β_i = 0.637 was assigned to all size classes. This value is close to the random close packing fraction of ideal monodisperse spheres [29]. Particle shape and packing history affect the reference packing state of actual powders [30,31]. The geometric density was calculated using the true density of pure LFP, ρ_s = 3.60 g·cm^{-3}:

$$\rho_{th} = \gamma \rho_s \tag{7}$$

The continuous particle size distribution was divided into four size classes using D_0, D_{10}, D_{50}, D_{90}, and D_{100} as boundaries. The corresponding solid volume fractions are 10%, 40%, 40%, and 10%. The representative diameter of each size class was taken as the geometric mean of the lower and upper bounds of the corresponding interval, as listed in Table 3.

Table 3 Particle size intervals, volume fractions, and representative diameters used in the geometric packing estimates

Size class	Size interval	Volume fraction y_i	LFP-1S (μm)	LFP-2S (μm)
1	D_{90}–D_{100}	0.10	5.34	10.67
2	D_{50}–D_{90}	0.40	1.98	3.96
3	D_{10}–D_{50}	0.40	0.99	1.29
4	D_0–D_{10}	0.10	0.55	0.62

Table 4 Comparison of geometric packing estimates and measured powder compaction densities

Sample	Estimated packing fraction γ	ρ_s (g·cm^{-3})	Estimated geometric density (g·cm^{-3})	Measured compaction density (g·cm^{-3})	Relative deviation
LFP-1S	0.710	3.60	2.56	2.52	+1.5%
LFP-2S	0.741	3.60	2.67	2.58	+3.4%

Equations (1)–(6) yield estimated packing fractions of approximately 0.710 and 0.741 for LFP-1S and LFP-2S, respectively. Under identical compaction conditions of 300 MPa and a 30 s holding time, the measured powder compaction densities are 2.52 and 2.58 g·cm^{-3}, respectively, corresponding to an increase of 0.06 g·cm^{-3} or approximately 2.4%. The geometric densities calculated using Eq. (7) are 2.56 and 2.67 g·cm^{-3}, respectively (Table 4). The four-size-class model gives a 4.37% increase in γ, compared with the measured compaction density increase of 2.4%. The relative deviations are +1.5% and +3.4%, respectively. The estimated and measured values follow the same trend, indicating that the coexistence of coarse and fine particles improves geometric packing efficiency.

3.3 Electrochemical performance of the once-sintered and re-sintered samples

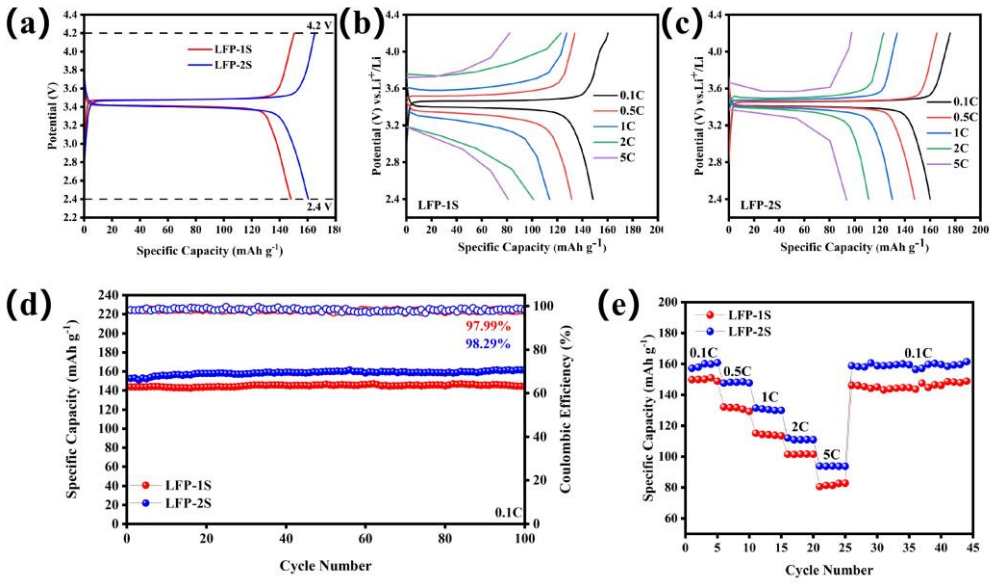

Fig. 4 Galvanostatic charge–discharge, rate capability, and cycling performance of LFP-1S and LFP-2S: (a) charge–discharge curves at 0.1 C; (b,c) charge–discharge curves of the two samples at 0.1, 0.5, 1, 2, and 5 C, respectively; (d) discharge specific capacities over 100 cycles at 0.1 C and initial Coulombic efficiencies; and (e) rate capability

Figure 4a presents the charge–discharge curves of LFP-1S and LFP-2S at 0.1 C. Both samples exhibit characteristic voltage plateaus near 3.4 V, associated with the Fe^{2+}/Fe^{3+} redox reaction coupled with Li^+ extraction and insertion. These features indicate that the principal electrochemical reaction characteristics of LFP are retained after re-sintering. LFP-2S delivers a discharge specific capacity of 160 mAh·g^{-1}, compared with 146 mAh·g^{-1} for LFP-1S, and exhibits a longer discharge plateau, demonstrating greater accessible capacity under the tested conditions.

Figures 4b and 4c compare the charge–discharge responses at different C-rates. As the rate increases from 0.1 to 5 C, the charge plateaus shift toward higher potentials and the discharge plateaus toward lower potentials, accompanied by increasing polarization and decreasing accessible capacity. Compared with LFP-1S, LFP-2S maintains more clearly defined discharge plateaus and higher discharge specific capacities at elevated C-rates, consistent with reduced polarization during high-rate operation. At 5 C, LFP-2S delivers 94 mAh·g^{-1}, compared with 82 mAh·g^{-1} for LFP-1S, corresponding to

an increase of approximately 14.6%. When the rate returns to 0.1 C, both samples recover capacities close to their initial low-rate values within the same rate test (Fig. 4e), demonstrating good capacity recovery after high-rate cycling.

Figure 4d shows the cycling performance at 0.1 C. During the initial cycles, LFP-2S exhibits a modest increase in discharge specific capacity before stabilizing, whereas LFP-1S remains comparatively stable. After 100 cycles, LFP-2S delivers a discharge specific capacity of 161 mAh·g^{-1}, compared with 145 mAh·g^{-1} for LFP-1S. The initial Coulombic efficiencies are 98.29% and 97.99% for LFP-2S and LFP-1S, respectively. These results demonstrate that LFP-2S maintains a higher reversible capacity throughout the cycling test.

Re-sintering increases the powder compaction density from 2.52 to 2.58 g·cm^{-3} while improving discharge specific capacity and rate capability. Despite its lower BET specific surface area and larger mean particle size, LFP-2S exhibits higher capacities at elevated C-rates and maintains stable capacity over 100 cycles at 0.1 C. These results demonstrate simultaneous improvements in powder packing and electrochemical performance following re-sintering.

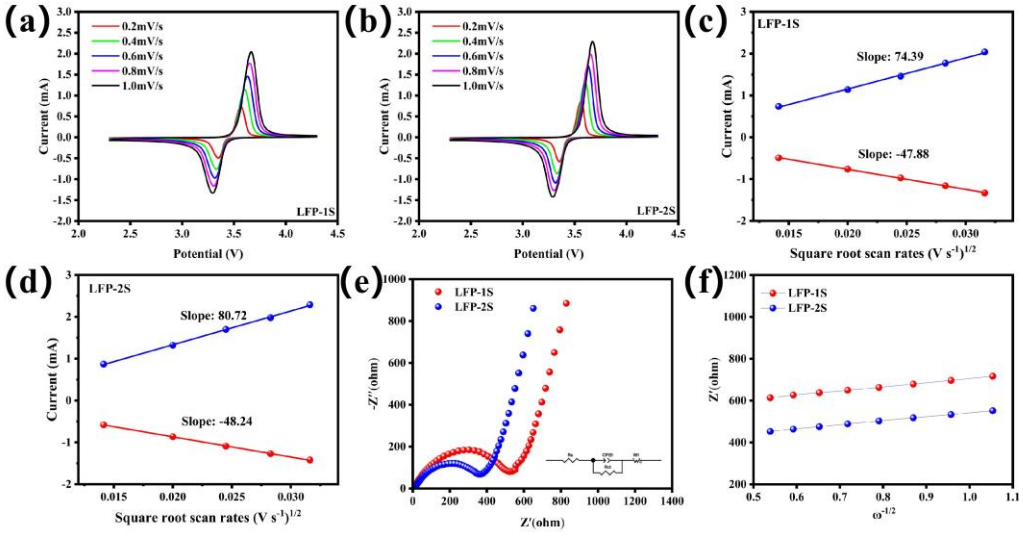

Fig. 5 CV and EIS analyses of LFP-1S and LFP-2S: (a,b) CV curves of the two samples at different scan rates, respectively; (c,d) linear fits of the corresponding oxidation and reduction peak currents against the square root of scan rate; (e) impedance spectra and equivalent circuit; and (f) linear fits of Z' against $\omega^{-1/2}$

Figure 5a,b shows the CV curves recorded at 0.2, 0.4, 0.6, 0.8, and 1.0 $mV \cdot s^{-1}$. Both samples exhibit one principal pair of redox peaks, corresponding to Li^+ extraction accompanied by Fe^{2+} oxidation and Li^+ insertion accompanied by Fe^{3+} reduction, consistent with the galvanostatic charge–discharge plateaus. With increasing scan rate, the peak currents increase, the oxidation peak shifts to more positive potentials, and the reduction peak shifts to more negative potentials, reflecting increased polarization. At the same scan rate, both the oxidation and reduction peak currents are higher for LFP-2S than for LFP-1S. These peak-current responses and the impedance results below are used to analyze differences in reaction kinetics between the samples.

The Randles–Ševčík relationship applicable near 298 K was used for the analysis [9,32]:

$$I_p = 2.69 \times 10^5 \, n^{\frac{3}{2}} \, A \, C_0 \, D_{Li+}^{\frac{1}{2}} \, v^{\frac{1}{2}} \quad (8)$$

Here, I_p is the peak current, n is the number of electrons transferred (n = 1 for $LiFePO_4$), A is the electrode area used in the calculation, C_0 is the solid-phase lithium concentration, D_{Li+} is the apparent Li^+ diffusion coefficient, and v is the scan rate. I_p, A, C_0, and v are expressed in A, cm^2, $mol \cdot cm^{-3}$, and $V \cdot s^{-1}$, respectively, giving a diffusion coefficient in $cm^2 \cdot s^{-1}$.

The oxidation and reduction peak currents I_p were plotted separately against the square root of scan rate $v^{1/2}$ (Fig. 5c,d). Both samples exhibit good linearity, indicating a diffusion-related contribution to the peak-current response over 0.2–1.0 $mV \cdot s^{-1}$. With peak currents expressed in mA and scan rates in $V \cdot s^{-1}$, the fitted oxidation and reduction slopes are 74.39 and −47.88 for LFP-1S and 80.72 and −48.24 for LFP-2S, respectively. Using identical area and concentration parameters in Eq. (8), the CV-derived apparent Li^+ diffusion coefficient associated with the oxidation peak increases from approximately 1.15×10^{-10} to 1.35×10^{-10} $cm^2 \cdot s^{-1}$. The increase calculated from the fitted slopes is approximately 17.7%. The magnitude of the reduction-peak slope increases from 47.88 to 48.24, corresponding to an approximately 1.5% increase in the apparent diffusion coefficient. EIS was subsequently used to analyze interfacial charge transfer and the low-frequency transport response. The

Nyquist plots in Fig. 5e consist of a depressed semicircle at high-to-intermediate frequencies and an extended low-frequency region. In the equivalent circuit, the series resistance represents ohmic contributions from the electrolyte and contacts, the semicircle is mainly associated with charge-transfer resistance and a nonideal interfacial capacitive response, and the low-frequency region includes mass-transport contributions. Under identical measurement states and the same equivalent-circuit interpretation, the smaller semicircle of LFP-2S corresponds to a lower apparent interfacial charge-transfer resistance. Benedek et al. related surface lithium dynamics to phase separation in LFP [33], whereas Wu et al. associated the improved high-rate performance after W coating with fast charge transfer near the particle surface [34]. These studies indicate that surface processes and bulk transport jointly influence the rate response of LFP.

To compare the low-frequency responses, Z' was fitted linearly against $\omega^{-1/2}$ over the selected interval (Fig. 5f). Using the semi-infinite Warburg approximation and treating the other circuit contributions as corresponding constant terms, the real part of the impedance and the apparent diffusion coefficient are expressed as follows [35–39]:

$$Z' = R_s + R_{ct} + \sigma_W \omega^{-1/2} \tag{9}$$

$$D_{Li^+} = \frac{R^2T^2}{2A^2n^4F^4C^2\sigma_W^2} \tag{10}$$

Here, Z' is the real part of the impedance (Ω), $\omega = 2\pi f$ is the angular frequency (rad·s^{-1}), σ_W is the Warburg coefficient (Ω·s$^{-1/2}$), R is the gas constant, T is the absolute temperature, F is the Faraday constant, and A and C are the electrode area and solid-phase lithium concentration used in the model, respectively. With A in cm^2 and C in mol·cm^{-3}, the resulting diffusion coefficient is expressed in cm^2·s^{-1}. The fitted slopes in Fig. 5f are 196.26 and 191.85 Ω·s$^{-1/2}$ for LFP-1S and LFP-2S, respectively. The EIS-derived apparent Li^+ diffusion coefficients D_{Li^+} calculated using Eq. (10) are 1.38×10^{-15} and 1.45×10^{-15} cm^2·s^{-1}, respectively. The increase calculated from the Warburg slopes is approximately 4.7%. The EIS-derived values are approximately five orders of magnitude lower than the CV-derived values. These parameters describe the model responses associated with low-frequency diffusion impedance and

scan-rate-dependent peak currents, respectively, and both show improved transport after re-sintering.

The CV and EIS results together show that re-sintering decreases the interfacial charge-transfer resistance and increases the apparent Li^+ diffusion coefficients. Despite the lower BET specific surface area, the electrode exhibits more favorable charge-transfer and Li^+ transport responses, consistent with its improved rate capability.

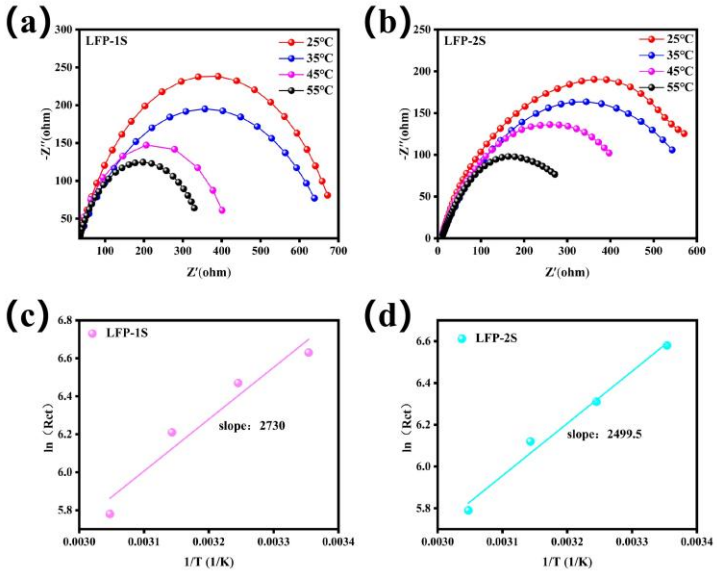

Fig. 6 Temperature-dependent EIS and Arrhenius analyses of LFP-1S and LFP-2S: (a,b) Nyquist plots of the two samples at 25, 35, 45, and 55 °C, respectively; and (c,d) corresponding linear fits of ln(R_{ct}) against 1/T

To examine the temperature dependence of the interfacial processes, EIS measurements were performed at 25, 35, 45, and 55 °C, as shown in Fig. 6a,b. With increasing temperature, the high-to-intermediate-frequency semicircles of both samples become smaller, reflecting thermally activated interfacial responses. At each measured temperature, the semicircle of LFP-2S is smaller than that of LFP-1S, indicating that its lower interfacial charge-transfer impedance is maintained throughout the investigated temperature range. The temperature dependence of the charge-transfer resistance was fitted using an approximate Arrhenius relationship over this narrow temperature interval [40]:

$$\ln(R_{ct}) = \frac{E_a}{RT} + C \quad (11)$$

Here, C is a fitting constant. The slopes of the ln(R_{ct}) versus 1/T fits in Fig. 6c,d are 2730 and 2499.5, yielding apparent activation energies of 22.7 and 20.8 kJ·mol^{-1} for LFP-1S and LFP-2S, respectively, a decrease of approximately 8.4%. The lower apparent activation energy reflects a more favorable thermally activated interfacial charge-transfer response in LFP-2S, consistent with its lower R_{ct} and improved rate capability.

LFP-2S exhibits both a lower apparent activation energy and a smaller impedance semicircle, indicating that re-sintering improves interfacial charge transfer and its temperature response. Together with the CV and room-temperature EIS results, the increase in apparent diffusion coefficients and decrease in interfacial impedance are consistent with the improvements in capacity and rate capability. At the particle scale, re-sintering produces a bimodal distribution containing coarse and fine particles and increases the measured powder compaction density by approximately 2.4%. In the electrode reaction, it decreases the interfacial charge-transfer resistance and lowers the apparent activation energy by approximately 8.4%. These results demonstrate the combined effects of the same heat-treatment procedure on geometric packing and electrochemical kinetics. Cho and Park improved both the degree of graphitization and cathode–electrolyte interfacial stability through carbon-layer functionalization and observed a lower charge-transfer resistance after cycling [41]. Their study further illustrates the combined influence of carbon-layer structure and interfacial chemistry on LFP kinetics.

4 Conclusions

LFP/C was prepared from $Fe_3(PO_4)_2$, Li_3PO_4, and glucose. Additional re-sinte ring of material from the same once-sintered batch revealed relationships among particle organization, powder packing, and electrochemical response. The main co nclusions are as follows.

(1) Re-sintering transforms a predominantly unimodal particle size distribution with a main mode at 1.16 μm into a bimodal distribution with modes at 1.19 and 6.19

μm. D_{50} increases from 1.33 to 1.98 μm, D_{90}/D_{10} increases from 4.01 to 9.36, and the BET specific surface area decreases from 13.88 to 9.554 $m^2 \cdot g^{-1}$. The four-size-class geometric packing model yields an increase in γ from 0.710 to 0.741, consistent with the increase in measured powder compaction density from 2.52 to 2.58 $g \cdot cm^{-3}$. The coexistence of coarse and fine particles provides a graded particle size distribution that promotes interstitial filling and improves geometric packing efficiency.

(2) The unit-cell volume increases from 290.373 to 291.191 $Å^3$. The CV-derived apparent Li^+ diffusion coefficient associated with the oxidation peak increases by approximately 17.7%, and the EIS-derived apparent Li^+ diffusion coefficient increases by approximately 4.7%. The interfacial charge-transfer resistance decreases, and the apparent activation energy decreases from 22.7 to 20.8 $kJ \cdot mol^{-1}$. The discharge specific capacity at 0.1 C increases from 146 to 160 $mAh \cdot g^{-1}$, the discharge specific capacity after 100 cycles increases from 145 to 161 $mAh \cdot g^{-1}$, and the discharge specific capacity at 5 C increases from 82 to 94 $mAh \cdot g^{-1}$. The initial Coulombic efficiency increases from 97.99% to 98.29%. The improved particle packing and electrode transport response demonstrate that re-sintering enhances both compaction density and electrochemical performance.

CRediT authorship contribution statement

Chang Liu: Writing – original draft, Software, Methodology, Investigation, Formal analysis, Data curation, Conceptualization.**Tingzhi Feng:** Formal analysis.**Fuliang Zhu:** Writing – review & editing, Validation, Supervision, Resources, Project administration, Funding acquisition, Formal analysis, Conceptualization. **Yanshuang Meng:** Writing – review & editing, Project administration, Funding acquisition, Conceptualization.

Data availability

The data supporting the findings of this study are available on request.

Competing interests

The authors declare that they have no known competing financial interests or personal relationships that could have influenced the work reported in this paper.

Acknowledgements

This work was supported by the National Natural Science Foundation of China (Grant No. 52064035) and the Key Research and Development Program of Gansu Province (Grant No. 25YFGA024).

References

[1] Padhi AK, Nanjundaswamy KS, Goodenough JB (1997) Phospho-olivines as positive-electrode materials for rechargeable lithium batteries. Journal of The Electrochemical Society 144:1188–1194. https://doi.org/10.1149/1.1837571

[2] Huang X, Worsley J, Pathirana T et al (2026) A perspective on five-generation high-energy-density $LiFePO_4$ cathodes and beyond: From materials to manufacturing. EcoEnergy e70123. https://doi.org/10.1002/ece2.70123

[3] Syed MA, Salehabadi M, Obrovac MN (2024) High energy density large particle $LiFePO_4$. Chemistry of Materials 36:803–814. https://doi.org/10.1021/acs.chemmater.3c02301

[4] Pikalova E, Il'ina E, Osinkin D (2026) The state-of-the-art in lithium iron phosphate $LiFePO_4$ synthesis: A review of methods and optimizations. Journal of Energy Storage 158:121759. https://doi.org/10.1016/j.est.2026.121759

[5] Yin L, Jiang Y, Wang J et al (2026) Comprehensive review of synthesis, structure, and electrochemical performance of $LiFePO_4$. Advanced Science 13:e77203. https://doi.org/10.1002/advs.77203

[6] Ishtiaq S, Majid A, Qadeer A et al (2025) Recent progress in carbon coating and surface modification of $LiFePO_4$ cathodes. RSC Advances 15:42331–42346. https://doi.org/10.1039/D5RA05833C

[7] Yang H, Wang Y, Li X et al (2025) Synthesis of high compaction density $LiFePO_4$/C cathode material with compound carbon source based on tannic acid and sophorolipid. Ionics 31:5411–5423. https://doi.org/10.1007/s11581-025-06305-1

[8] Yang H, Guo J, Xue J et al (2026) Preparation of high-density lithium iron phosphate with Nb, Ti, V co-doping and non-uniform particle distribution. Ionics 32:1849–1862. https://doi.org/10.1007/s11581-025-06915-9

[9] Kang T, Meng Y, Liu X (2025) Optimizing lithium-ion diffusion in $LiFePO_4$: The impact of Ti^{4+} doping on high-rate capability and electrochemical stability. Ionics 31:2419–2428. https://doi.org/10.1007/s11581-025-06075-w

[10] Prosini PP, Lisi M, Zane D et al (2002) Determination of the chemical diffusion coefficient of lithium in $LiFePO_4$. Solid State Ionics 148:45–51. https://doi.org/10.1016/S0167-2738(02)00134-0

[11] Su B, Liu Y, Yu A (2026) Optimizing electrochemical performance of $LiFePO_4$ through synergistic modulation of sintering temperature and Li/Fe ratio under constant grain size. ACS Applied Energy Materials 9:485–495. https://doi.org/10.1021/acsaem.5c03273

[12] Ding R, Zheng Y, Liang G (2026) The effect of $Fe_3(PO_4)_2 \cdot 8H_2O$ precursor morphology on the performance of $LiFePO_4$/C cathode materials. Ionics 32:7551–7561. https://doi.org/10.1007/s11581-026-07220-9

[13] Ke H, He Y, Tang J et al (2026) A new approach to synthesize $LiFePO_4$/C cathode with improved compacted density and enhanced electrochemical performance. ACS Sustainable Chemistry & Engineering 14:15812–15824. https://doi.org/10.1021/acssuschemeng.6c05327
[14] Liu S, Zhao Y, Ma T et al (2026) Pre-agglomeration granulation for fluidized bed sintering of Geldart Group C $LiFePO_4$ with enhanced electrochemical performance. Small Methods e71063. https://doi.org/10.1002/smtd.71063
[15] Han T, Son CS, Kim Y et al (2026) Hydrothermal synthesis of high-performance carbon-free $LiFePO_4$ cathodes for lithium-ion batteries under temperature-controlled conditions. International Journal of Electrochemical Science 21:101395. https://doi.org/10.1016/j.ijoes.2026.101395
[16] Wang Y, Zhang J, Xue J et al (2021) $LiFePO_4$/C composites with high compaction density as cathode materials for lithium-ion batteries with high volumetric energy density. Ionics 27:4687–4694. https://doi.org/10.1007/s11581-021-04078-x
[17] Li P, Wang Y, Zhu L et al (2025) Particle size grading strategy for enhanced performance of lithium iron phosphate cathode materials. Crystals 15:308. https://doi.org/10.3390/cryst15040308
[18] Kubarkov AV, Babkin AV, Drozhzhin OA et al (2023) Engendering high energy density $LiFePO_4$ electrodes with morphological and compositional tuning. Nanomaterials 13:1771. https://doi.org/10.3390/nano13111771
[19] Lei J, Huang H, Zhang L et al (2026) Theoretical criteria for particle size distribution of high compacted density $LiFePO_4$ based on packing density modeling. Particuology 117:524–533. https://doi.org/10.1016/j.partic.2026.08.017
[20] Wang J, Shen Z, Yi M (2019) Hydraulic compaction on electrode to improve the volumetric energy density of $LiFePO_4$/graphite batteries. Industrial & Engineering Chemistry Research 58:15407–15415. https://doi.org/10.1021/acs.iecr.9b01530
[21] Zhu R, Liu G, Qu G et al (2024) Enhancing volumetric energy density of $LiFePO_4$ battery using liquid metal as conductive agent. Advanced Functional Materials 34:2409230. https://doi.org/10.1002/adfm.202409230
[22] Syed MA, Obrovac MN (2026) Ultra-high density $LiFePO_4$ electrodes. Journal of The Electrochemical Society 173:030509. https://doi.org/10.1149/1945-7111/ae3b77
[23] Kim J, Kim M, Han S et al (2026) Development of nano-sized $LiFePO_4$ dry cathodes with enhanced flexibility and mechanical robustness for roll-to-roll dry coating process. Microstructures 6:2026051. https://doi.org/10.20517/microstructures.2025.59
[24] Vankani C, Arifiadi A, Yan P et al (2026) Enabling stable high-rate cycling of energy dense lithium-ion batteries ($LiFePO_4$ || graphite) based on thick electrodes by employing ester-based electrolytes. Advanced Energy and Sustainability Research 7:e70233. https://doi.org/10.1002/aesr.70233
[25] Kumar D, Tripathy A, Sharma M et al (2026) Enhanced kinetics in Cu-doped $LiFePO_4$ cathodes due to local structural disorder. Communications Materials 7:185. https://doi.org/10.1038/s43246-026-01092-2
[26] Stovall T, de Larrard F, Buil M (1986) Linear packing density model of grain mixtures. Powder Technology 48:1–12. https://doi.org/10.1016/0032-5910(86)80058-4
[27] de Larrard F (1999) Concrete Mixture Proportioning: A Scientific Approach. E & FN Spon, London. https://doi.org/10.1201/9781482272055
[28] Rettinger C, Tabesh M, Rüde U et al (2023) On the use of packing models for the prediction of fluvial sediment porosity. Earth Surface Dynamics 11:1097–1115. https://doi.org/10.5194/esurf-11-1097-2023

[29] Torquato S, Stillinger FH (2010) Jammed hard-particle packings: From Kepler to Bernal and beyond. Reviews of Modern Physics 82:2633–2672. https://doi.org/10.1103/RevModPhys.82.2633
[30] Yu AB, Zou RP, Standish N (1996) Modifying the linear packing model for predicting the po rosity of nonspherical particle mixtures. Industrial & Engineering Chemistry Research 35:3730–37 41. https://doi.org/10.1021/ie950616a
[31] Cho G-C, Dodds J, Santamarina JC (2006) Particle shape effects on packing density, stiffness , and strength: Natural and crushed sands. Journal of Geotechnical and Geoenvironmental Enginee ring 132:591–602. https://doi.org/10.1061/(ASCE)1090-0241(2006)132:5(591)
[32] Bard AJ, Faulkner LR (2001) Electrochemical Methods: Fundamentals and Applications, 2nd edn. John Wiley & Sons, New York
[33] Benedek P, Zhao X, Bileter ER et al (2026) Surface coatings to mitigate phase separation in $LiFePO_4$ during lithium-ion battery discharge. Matter 9:102725. https://doi.org/10.1016/j.matt.2026. 102725
[34] Wu K, Fang J, Zhang W et al (2026) Atomic layer deposited conductive tungsten coating en abling ultrahigh-rate capability for commercial $LiFePO_4$ cathodes. Journal of Materials Chemistry A 14:27050–27060. https://doi.org/10.1039/D6TA02427K
[35] Tuo K, Mao L, Ding H et al (2021) Boron and phosphorus dual-doped carbon coating impro ves electrochemical performances of $LiFe_{0.8}Mn_{0.2}PO_4$ cathode materials. ACS Applied Energy Mat erials 4:8003–8015. https://doi.org/10.1021/acsaem.1c01318
[36] Hwang J, Kong KC, Chang W et al (2017) New liquid carbon dioxide based strategy for hig h energy/power density $LiFePO_4$. Nano Energy 36:398–410. https://doi.org/10.1016/j.nanoen.2017.0 4.046
[37] Cao Y, Duan J, Hu G et al (2013) Synthesis and electrochemical performance of nanostructur ed $LiMnPO_4$/C composites as lithium-ion battery cathode by a precipitation technique. Electrochim ica Acta 98:183–189. https://doi.org/10.1016/j.electacta.2013.03.014
[38] Yang L, Wang Y, Wu J et al (2017) Facile synthesis of micro-spherical $LiMn_{0.7}Fe_{0.3}PO_4$/C ca thodes with advanced cycle life and rate performance for lithium-ion battery. Ceramics Internation al 43:4821–4830. https://doi.org/10.1016/j.ceramint.2016.12.025
[39] Liu H, Ren L, Li J et al (2016) Iron-assisted carbon coating strategy for improved electroche mical $LiMn_{0.8}Fe_{0.2}PO_4$ cathodes. Electrochimica Acta 212:800–807. https://doi.org/10.1016/j.electac ta.2016.07.049
[40] Liao L, Zuo P, Ma Y et al (2012) Effects of temperature on charge/discharge behaviors of Li $FePO_4$ cathode for Li-ion batteries. Electrochimica Acta 60:269–273. https://doi.org/10.1016/j.electa cta.2011.11.041
[41] Cho JW, Park YJ (2026) Heteroatom-mediated functional carbon engineering for the simultan eous enhancement of graphitization and interfacial stability in $LiFePO_4$. ACS Applied Energy Mat erials 9:13763–13777. https://doi.org/10.1021/acsaem.6c02899